VIROLOGY

Enhanced packaging of U6 small nuclear RNA and splicing-related proteins into extracellular vesicles during HIV infection

Yiyao Huang[1,2], Ahmed Abdelgawad[3], Olesia Gololobova[2], Zhaohao Liao[2], Xinyu Cong[4], Mona Batish[3], Lei Zheng[1]*, Kenneth W. Witwer[2,5,6]*

U6 small nuclear RNA (U6 snRNA), a critical spliceosome component primarily found in the nucleus, plays a vital role in RNA splicing. Our previous study, using the simian immunodeficiency virus (SIV) macaque model, revealed an increase of U6 snRNA in plasma extracellular vesicles (EVs) in acute retroviral infection. Given the limited understanding of U6 snRNA dynamics across cells and EVs, particularly in SIV infection, this research explores U6 snRNA trafficking and its association with splicing proteins in the nucleus, cytoplasm, and EVs. We observed a redistribution of U6 snRNA from the nucleus to EVs post-infection, accompanied by distinct protein profile changes and alterations in nucleic acid metabolism and spliceosome pathways. In addition, U6 machinery proteins changed in cells and EVs in a contrasting manner. The redistribution of U6 and related proteins we observed could be part of a viral strategy to redirect host splicing machinery, suggesting that U6 may have regulatory roles and be part of retroviral infection signature.

INTRODUCTION

Extracellular vesicles (EVs) are nanosized membranous vesicles released from most cells, playing crucial roles in intercellular communication (*1*, *2*). They have emerged as critical factors in HIV pathogenesis and host-virus interactions, functioning similarly to retroviruses by transporting various bioactive molecules between cells, including both host and viral components (*3*–*5*). EVs encapsulate diverse RNA species, such as mRNAs (*6*, *7*), microRNAs (miRNAs) (*8*, *9*), and other noncoding RNAs (*10*, *11*), alongside viral RNA fragments (*12*). Recent research indicates that these RNAs within EVs from different sources can either facilitate or inhibit HIV infection (*13*). Our group's latest high-throughput sequencing studies also identified EV-associated RNA profiles involved in immune regulation and inflammatory responses in HIV infection (*14*).

HIV manipulates host cellular machinery to integrate its genetic material into the host's genome, producing spliced and unspliced mRNA forms essential for viral protein production and replication (*15*, *16*). In addition, HIV also alters the splicing patterns of host genes, leading to altered gene and RNA levels in both host cells (*8*, *17*) and the EVs (*14*, *18*, *19*) they release. Evidence indicates that HIV also encapsulates host RNAs. Several polymerase III (Pol III) transcripts such as Y RNAs, 7SK RNA, U6 snRNA, and cellular mRNAs are reported to be selectively enriched in HIV-1 particles (*20*–*22*). Given their overlapping contents and physical characteristics, distinguishing between EVs and virions (or "host EVs" and "viral EVs") after release can be challenging (*23*, *24*). Consequently, RNAs that have previously been reported in association with EVs or virions may not be specific to either class of particle.

Previously, we revealed an association between plasma EV U6 small nuclear RNA (U6 snRNA) levels and the viral peak during acute SIV infection in pigtailed macaques (*Macaca nemestrina*) coinoculated with the neurovirulent SIV-17EFr clone and the immunosuppressive SIV-B670 swarm (*18*). Although several studies have indicated alterations in EV-associated U6 snRNA in cancer (*25*–*27*), the dynamics of EV U6 snRNA in other disease states, including viral infection, remain largely unexplored. As a crucial spliceosome component typically located in the nucleus, U6 snRNA is also known to interact transiently with ribonucleoproteins (*28*) or U bodies (*29*) in the cytoplasm. Since U6 snRNAs play a vital role in pre-mRNA splicing (*30*, *31*), particularly in catalyzing splicing reactions after spliceosome assembly, changes in the quantities and localization of U6 snRNAs may contribute to altered transcript alternative splicing and increased intron retention (*31*) during HIV infection. Furthermore, the release of these RNAs into EVs is still poorly defined.

Our study thus aims to elucidate how U6 snRNA and its associated proteins are distributed across various cellular compartments and EVs in retroviral infection. In SIV-17EFr– and SIV-B670–infected human CEMx174 cells, we noted a unique distribution pattern of U6 snRNA, marked by its reduction in the nucleus and increase in EVs. This pattern was specifically found in SIV and not in hepatitis B virus (HBV) infection. Additionally, changes in proteins related to nucleic acid metabolism, spliceosome pathways, and U6 snRNA machinery were detected in both the nucleus and EVs of SIV-infected cells. These findings suggest that retroviruses like HIV and SIV may use a strategy to redirect the host splicing machinery from the nucleus to EVs during infection, potentially affecting RNA splicing and the viral life cycle. This study thus provides valuable insights

[1]Department of Laboratory Medicine, Guangdong Provincial Key Laboratory of Precision Medical Diagnostics, Guangdong Engineering and Technology Research Center for Rapid Diagnostic Biosensors, Guangdong Provincial Key Laboratory of Single-cell and Extracellular Vesicles, Nanfang Hospital, Southern Medical University, Guangzhou, Guangdong, China. [2]Department of Molecular and Comparative Pathobiology, Johns Hopkins University School of Medicine, Baltimore, MD, USA. [3]Department of Medical and Molecular Sciences, University of Delaware, Newark, DE, USA. [4]Division of Biostatistics and Bioinformatics, Department of Environmental and Public Health Sciences, University of Cincinnati, Cincinnati, OH, USA. [5]Department of Neurology, Johns Hopkins University School of Medicine, Baltimore, MD, USA. [6]Richman Family Precision Medicine Center of Excellence in Alzheimer's Disease, Johns Hopkins University School of Medicine, Baltimore, MD, USA.
*Corresponding author. Email: kwitwer1@jhmi.edu (K.W.W.); nfyyzhenglei@smu.edu.cn (L.Z.)

into the interplay between HIV infection and cellular RNA processing mechanisms.

RESULTS

Characterization of EVs derived from uninfected and SIV-infected cells

Infection of CEMx174 cells with SIV-17EFr and SIV-B670 resulted in a decrease in cell viability 3 days post-infection, with the reduction being more pronounced in SIV-B670–infected cells (fig. S1A). The infectivity of virions produced from these cells, assessed by measuring luciferase activity in Tat-responsive LuSIV indicator cells (*32*), increased progressively for both viral strains, with SIV-B670 showing consistently higher luciferase activity induction compared with SIV-17EFr from day 1 to day 3 post-infection (fig. S1B).

EVs from uninfected (UI), SIV-17EFr–infected, and SIV-B670–infected cells were separated and characterized. Medium processing controls (MC) were included to assess potential contamination of proteins and bovine serum–derived EVs from the cell culture medium (CCM). Particle counts of EVs were normalized based on both particles per million viable cells and milliliter (ml) of medium. More particles were observed in the three B670-infected samples compared with the UI samples, although the difference did not reach statistical significance due to the small sample size and high variability (Fig. 1A, left). The MC showed a significantly lower particle concentration (particles/ml medium) compared with EVs (Fig. 1A, right). Particle size distribution analysis revealed a higher number of smaller particles from B670-infected cells (Fig. 1B). Transmission electron microscopy (TEM) images revealed oval/round particles consistent with EV morphology, as well as smaller protein aggregates in all groups (Fig. 1C). The levels of proteins that are commonly reported to be associated with intracellular components, fetal bovine serum (FBS), EVs, and immune cells were examined by mass spectrometry (MS) (Fig. 1D). Intracellular proteins were more enriched in the cytoplasm than in EVs and MC in all three groups. Conversely, EV general and immune cell proteins were more enriched in EVs than cytoplasm and MC. FBS markers were highly enriched in MC compared with cytoplasm and EVs.

The levels of canonical EV surface markers CD9, CD63, and CD81 were detected on EVs and MC by MACSplex (Fig. 1E) and single-particle interferometric reflectance imaging sensor (SP-IRIS) (Fig. 1F and fig. S2) platforms to evaluate EV presence and

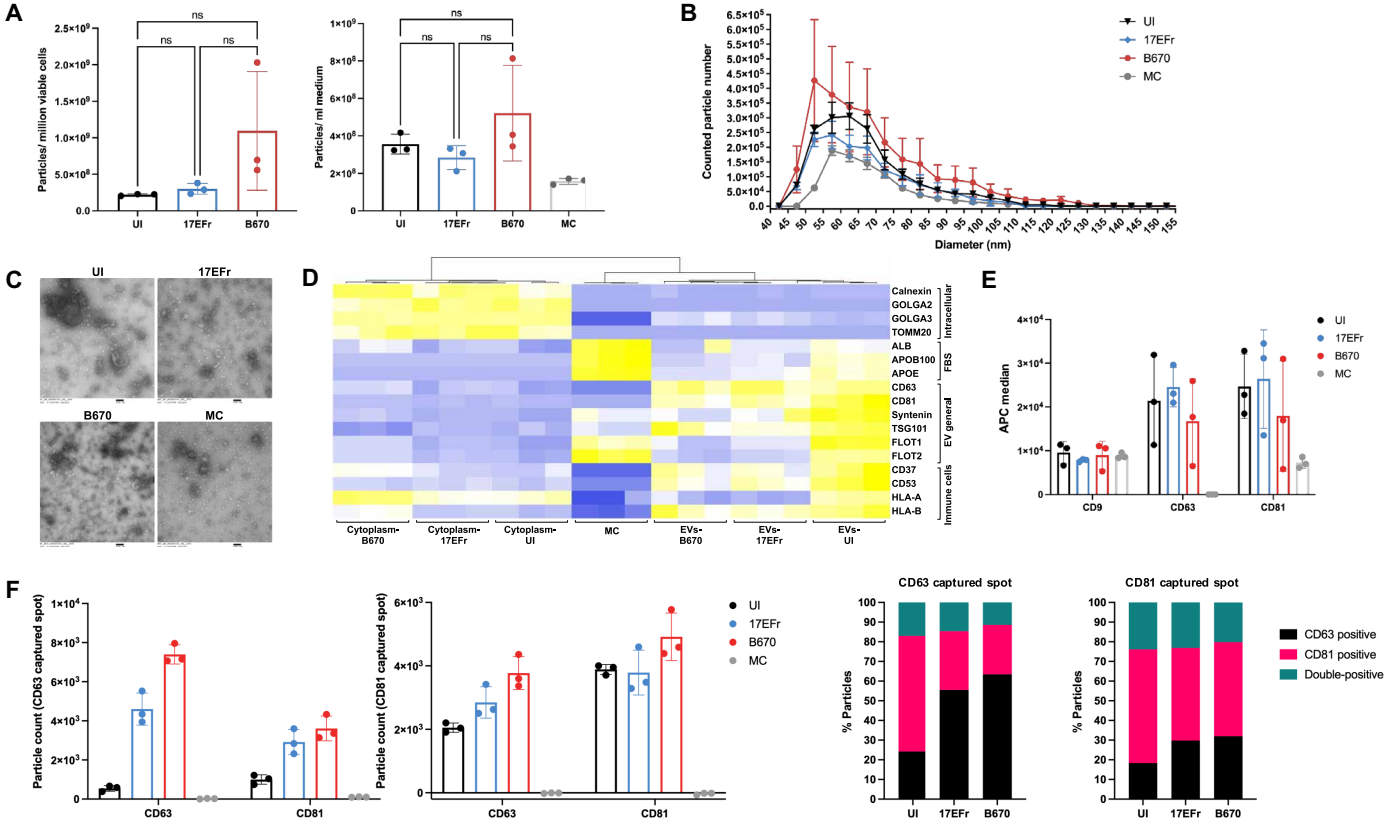

Fig. 1. Characterization of EVs from uninfected and SIV-infected cells. (**A**) Particle concentrations of EV preparations from UI, SIV-17EFr–infected, and SIV-B670–infected cells were measured by NFCM. Particle concentration for each group was normalized by particles per million viable cells (left) and per milliliter of CCM (right). (**B**) Size distributions of EVs (uninfected and infected) were measured by NFCM and presented as particle numbers in specific size ranges. (**C**) EVs and MC were visualized by negative staining TEM (scale bar, 100 nm). TEM is representative of 10 images taken of each sample from three independent samples. (**D**) Unsupervised hierarchical clustering of cytoplasm, EVs, and MC samples based on the levels of intracellular, FBS, EV, and immune cell–related markers. (**E**) The levels of CD9, CD63, and CD81 in EV and MC samples were detected by MACSplex. (**F**) Fluorescence detection of CD63 and CD81 on EVs captured by CD63 (left) and CD81 (right) antibody spots using SP-IRIS. The percent of CD63, CD81, and double-positive particles were calculated versus the total particle number captured on each spot. [(A) to (F)] Data are presented as mean ± SD. ns (no significant difference, $P > 0.05$), $^*P \leq 0.05$ by unpaired *t* test.

characteristics. CD63 and CD81 were significantly more abundant in EVs compared with MC, while CD9 exhibited similar levels in both, indicating an association of CD9 with CCM contamination (Fig. 1E and fig. S2). Furthermore, particles captured on the SP-IRIS chip through CD63 and CD81 were subsequently probed with fluorescently labeled CD63 and CD81 antibodies to confirm EV subtype differences based on tetraspanin profiles between uninfected and infected cells (Fig. 1F). More signal for both CD63 and CD81 was observed in B670 EVs when captured on CD63 and CD81 captured spots, respectively. Additionally, more captured particles were positive for either CD63 or CD81, while a small percentage exhibited dual positivity for both CD63 and CD81 in all samples.

U6 snRNA level and distribution alteration post-SIV infection: Increased in EVs and reduced in the nuclei

RNA concentrations of EVs and cell fractions were measured and normalized to ensure consistent RNA input within each batch for the subsequent quantitative polymerase chain reaction (qPCR) assays (fig. S3A). The levels of U6 and U1 snRNAs were assessed using the SYBR-based qPCR method in EVs obtained from UI, cells infected with SIV-17EFr and SIV-B670, and in the MC (Fig. 2A and fig. S3B). Both U6 and U1 snRNAs were significantly lower in MC, amplifying at approximately five cycles later on average (equivalent to a 32-fold reduction) compared with EVs, indicating minimal snRNA contribution from the CCM (fig. S3B). The abundance of EV U6 snRNAs was significantly higher in both 17EFr and B670 compared with UI, while U1 snRNA levels were similar (Fig. 2A). The elevated abundance of U6 snRNA following SIV infection was confirmed by both TaqMan- and SYBR-based qPCR methods, with an average fold change >3 for both virus strains (Fig. 2B). Additionally, U6 and U1 snRNA levels were found to be higher in EVs from HIV Rf– and BAL-infected cells versus UI by the TaqMan-based qPCR method (fig. S4).

To determine whether SIV infection affects the cellular abundance and localization of snRNAs, uninfected and infected cells were fractionated into cytosolic and nuclear fractions. Distribution of tubulin and glyceraldehyde-3-phosphate dehydrogenase (GAPDH) (cytoplasm) and lamin B (nucleus) confirmed successful separation (fig. S5). Both U6 and U1 snRNAs exhibited significantly lower abundance in the nuclei of cells infected with 17EFr and B670, with no difference in the cytoplasm, as measured by the SYBR-based qPCR method (Fig. 2C). The reduction of U6 snRNA in the nucleus was further confirmed using the TaqMan-based qPCR method (fig. S3C). Cq values were then normalized to the geometric mean of internal reference miRNAs (miR-29a, miR-342, and miR-181a) for additional validation (fig. S3D). Colocalization analysis of U6 snRNA and DAPI (4′,6-diamidino-2-phenylindole) staining (nuclear DNA) showed a reduction in the overlapping signal between U6 snRNA and DAPI signals post-infection with both virus strains (Fig. 2D).

HBV-infected plasma EVs were also assessed to determine whether the elevation of EV U6 snRNA is a phenomenon common to bloodborne viruses. Despite a higher concentration of particles in EV preparations from HBV-infected plasma with a higher viral load (10×10^8 copies/ml) (fig. S6, A and B), the level of U6 snRNA remained similar among uninfected individuals, HBV patients with a lower viral load (10×10^3 copies/ml), and those with a higher viral load (fig. S6C).

SIV infection and proteins in cytoplasm, nucleus, and EVs

We subsequently used label-free MS to explore protein profile alterations following SIV infection in the cytoplasm, nuclei, and EVs, seeking potential explanations for the observed changes in U6 snRNA. Proteins (3158, 28.6%) were detected in all three compartments, 2339 proteins (21.2%) were found in both the cytoplasm and nuclei, and a subset of proteins was exclusively detected in a single fraction (Fig. 3A). Gene ontology (GO) analyses by STRING were used to determine cellular compartments (Fig. 3B, left) and biological processes (Fig. 3B, right) associated with fraction-exclusive proteins. Proteins exclusive to EVs were primarily enriched for terms associated with vesicles, EVs, and the extracellular matrix. Terms such as cytoplasm and cytosol were enriched in both EVs and cytoplasm, while organelle-related terms and intracellular anatomical structures were enriched in both cytoplasm and nucleus. Mitochondria and organelle membrane terms were specifically enriched in cytoplasm, whereas nucleus-related terms like nuclear lumen and nucleoplasm were exclusively enriched in nucleus (Fig. 3B, left). Additionally, proteins exclusively detected in different fractions showed enrichment for distinct functions. For instance, metabolic processes were enriched in the cytoplasm, DNA and RNA processes in the nucleus, and multiple cellular processes in EVs (Fig. 3B, right).

Principal components analysis (PCA) of the proteome revealed distinct separation among various fractions, including cytoplasm, nucleus, EVs, and MC. Within each fraction, the proteome of UI samples exhibited a separation from both infected groups (Fig. 3C). Differentially expressed (DE) proteins in response to SIV infection were further examined in the cytoplasm, nuclei, and EVs (Fig. 3D). Nuclei exhibited the greatest number of proteins with altered abundance, followed by EVs. Comparing the two virus strains, B670 infection induced a higher number of altered proteins than 17EFr, but with a substantial portion of them being common to both virus strains. The DE proteins induced by both virus strains were visualized to show unique and overlapping proteins among three fractions by UpSetR analysis (Fig. 3E). Most of these proteins were exclusively identified in a single fraction, with a small subset demonstrating overlap between fractions. These included proteins that exhibited higher abundance in SIV infection, with 136 overlapping cytoplasm and nuclei and 108 in EVs and nuclei. GO biological process enrichment revealed that all of these proteins were associated with metabolic pathways. Additionally, proteins increased in infected nuclei and EVs were linked to nucleic acid processing terms, including RNA transportation and DNA replication.

Proteins related to nucleic acid metabolic and spliceosome pathways in SIV-infected nucleus and EVs

Considering that most proteins affected by SIV infection showed alterations exclusively in one fraction, we used a stepwise pipeline (Fig. 4A) to identify potential pathways associated with DE proteins in the cytoplasm, nucleus, and EVs. DE proteins in the three fractions were clustered into protein modules using weighted gene correlation network analysis (WGCNA), and these modules were further interpreted through protein-protein interaction (PPI) networks. Specifically, 5, 16, and 10 correlation modules were constructed in the cytoplasm, nucleus, and EVs, respectively, based on DE gene expression levels. Distinct color labels assigned by the WGCNA software were used to differentiate these modules, as shown in Fig. 4 (B to D). The proteins associated with each module are listed in table S1.

To explore the physiological significance of the color-labeled modules and explore their correlation with U6 snRNA differences, WGCNA was used to calculate their correlation with sample traits, including SIV infection, U6 snRNA level, and EV count (Fig. 4, B to

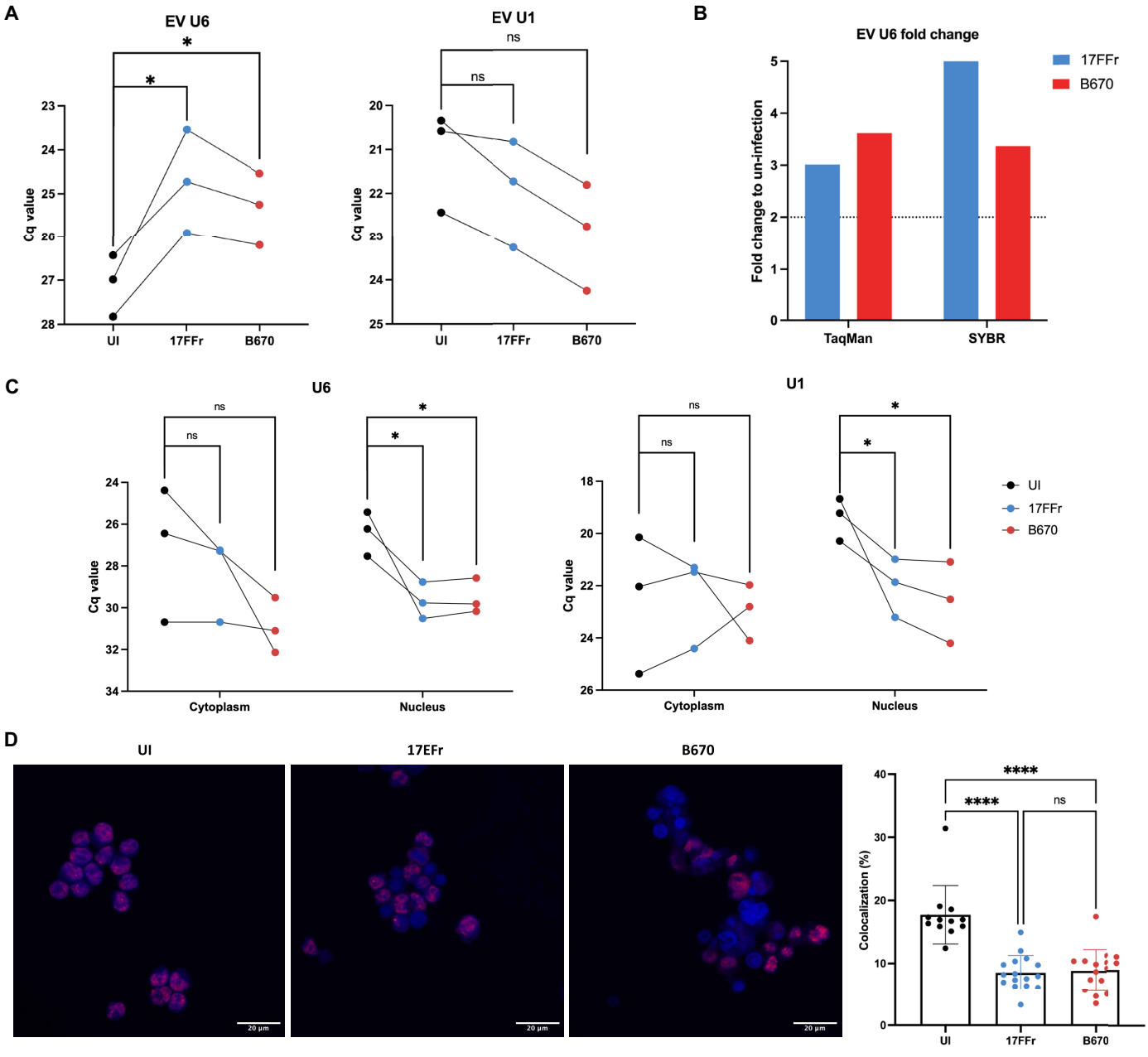

Fig. 2. U6 and U1 snRNA detection in cell fractions and EVs during SIV infection. (**A**) qPCR validation of U6 (left) and U1 snRNA (right) in EVs from UI, cells infected with SIV-17EFr and B670, and in MC using the SYBR-based qPCR method. Lines connect data points within each batch to illustrate results using equal RNA amounts. (**B**) Fold change of EV U6 snRNA in infection compared with no infection using TaqMan- and SYBR-based qPCR methods. (**C**) qPCR validation of U6 (left) and U1 (right) snRNAs in cytoplasm and nucleus of UI, 17EFr-infected, and B670-infected groups using the SYBR-based qPCR method. Lines connect data points within each batch to illustrate results using equal RNA amounts. (**D**) Confocal microscopy images (scale bar, 20 μm; magnification, ×40) of uninfected and infected cells stained with TR for U6 snRNA and DAPI for nuclear DNA. Imaris was used to identify and count voxels, where TR and DAPI signals overlap. The number of colocalized voxels was quantified, and the percentage of colocalized voxels relative to the total number of voxels in the defined cell area (Colocalization %) was calculated and presented. [(A) to (D)] Data are presented as mean ± SD. ns (no significant difference, $P > 0.05$), *$P \leq 0.05$, ****$P \leq 0.0001$ by unpaired *t* test.

D, left panels). In the cytoplasm, all protein modules displayed a significant correlation ($P < 0.05$) with SIV infection but were not significantly correlated with U6 snRNA levels ($P > 0.05$) (Fig. 4B, left panels). In the nuclei, all protein modules exhibited significant correlations with both SIV infection and U6 snRNA levels. Notably, modules positively correlated with SIV infection ($r > 0$) had a negative correlation with U6 snRNA levels ($r < 0$), whereas modules negatively correlated with SIV infection showed a positive correlation with U6 levels (Fig. 4C, left panels). For EVs, all modules exhibited a significant correlation with SIV infection, with 6 of 10 also correlated with U6 snRNA levels, while none showed a correlation with EV count. In contrast with the nuclei, modules positively or negatively

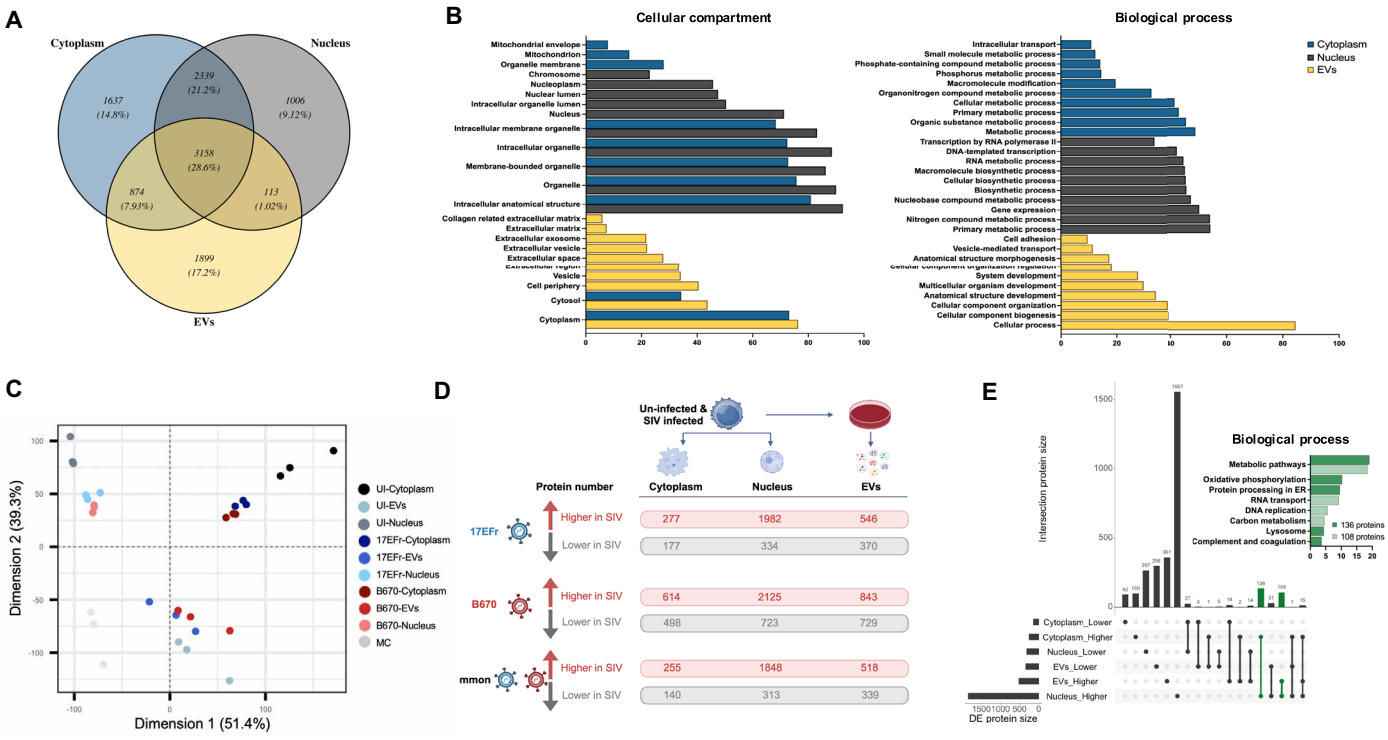

Fig. 3. Proteomic differences in SIV infection in cytoplasm, nucleus, and EVs. (**A**) Venn diagrams of all proteins identified by proteomics in cytoplasm, nucleus, and EVs. (**B**) Top 10 cellular compartments and biological processes ranked by identified exclusive protein number in the cytoplasm, nucleus, and EVs by the STRING. (**C**) PCA based on the proteome of samples. (**D**) Number of DE proteins in SIV-17EFr and B670 infection compared with uninfected groups in cytoplasm, nucleus, and EVs. (**E**) The UpSetR analysis presents DE proteins across cytoplasm, nucleus, and EVs. Each row represents a different comparison, with intersections marked by black dots connected by vertical lines in the matrix. The bottom charts show the total DE proteins in each comparison, while the top charts indicate the number of proteins overlapping between comparisons. STRING enrichment analysis identified biological processes associated with proteins dysregulated in the intersection of cytoplasm and nucleus and nucleus and EVs.

correlated with SIV infection also exhibited a corresponding positive/negative correlation with U6 snRNA levels (Fig. 4D, left panels).

Significant modules, with a correlation coefficient > 0.9 (versus SIV infection), were selected for pathway enrichment analysis across all three fractions (Fig. 4, B to D, right panels). Comparing common pathways in the three fractions, modules positively correlated with SIV infection (colored yellow) in the cytoplasm and nucleus were enriched for metabolic processes and immune system processes. Modules negatively correlated with SIV infection (colored blue) in the cytoplasm and nucleus but positively correlated with SIV infection in EVs were enriched for nucleic acid metabolic processes, particularly spliceosome, RNA transport, and mRNA surveillance pathways in both the nucleus and EVs. DE proteins enriched for common pathways between EVs and cells exhibited opposite changes in response to SIV infection in EVs compared with both cytoplasm and nucleus (Fig. 4E). Given that U6 snRNA is a crucial component of the spliceosome, we uncovered potential U6 snRNA–related proteins affected by SIV infection by identifying PPI networks for the spliceosome pathway, in both the nucleus ($n = 9$, purple and light cyan modules) and EVs ($n = 35$, yellow, green, and turquoise modules) (Fig. 4F).

U6 snRNA machinery proteins in SIV-infected cells and EVs

Proteins reported to regulate U6 snRNA cellular level and location were further detected in both cells and EVs through proteomic analysis (Fig. 5A) and Western blot (WB) (Fig. 5B and fig. S7). On the basis of proteomics data, $\log_2$ fold change (infected versus uninfected) was calculated for LSM1, LSM8, USP39, SART3, SMN, DIS3, and CD63 for cytoplasm, nucleus, and EVs (Fig. 5A). Most of these proteins exhibited opposite changes in EVs compared with both cytoplasm and nucleus following SIV infection, including LSM8 (up-regulated in EVs but down-regulated in the nucleus), USP39, SART3, and DIS3 (up-regulated in EVs but down-regulated in the cytoplasm), and CD63 (down-regulated in EVs but up-regulated in cytoplasm and nucleus). SMN was significantly down-regulated only in the cytoplasm. Further WB analysis of whole-cell lysate, cytoplasm, and nucleus fractions confirmed the dysregulation of LSM8, USP39, SART3, SMN, DIS3, and CD63 in response to SIV infection (Fig. 5B). While proteomics indicated the presence of these U6 snRNA machinery proteins in EVs, WB analysis detected LSM1, DIS3, and CD63 (fig. S7), but not SMN and LSM8, possibly due to antibody sensitivity and limitations in sample volume (since most EV samples were used for proteomics). Of the 37 EV surface proteins related to potential cellular sources examined using the MACSplex platform, five showed significant differences between infected and uninfected states (Fig. 5C). Specifically, T cell and B cell markers CD4 and CD19 decreased in infection, indicating that cell death limited EV release from these specific cell types. Conversely, immune activation–related markers CD69, CD2, and CD25 increased on the surface of EVs, reflecting potential changes in the immune cell response.

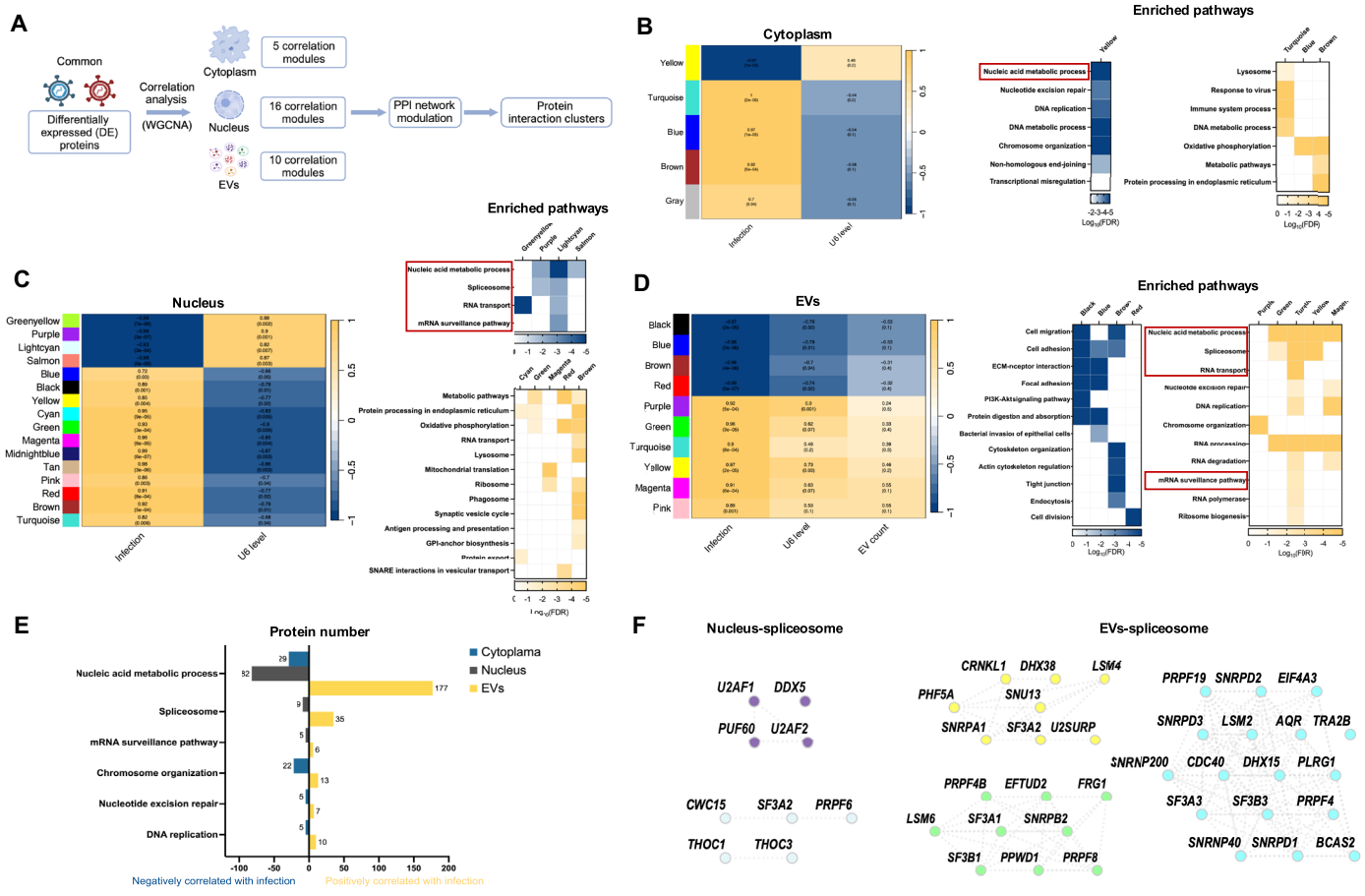

Fig. 4. Protein profiling of SIV infection reveals nucleic acid metabolic and spliceosome pathways. (**A**) Bioinformatics pipeline for DE protein correlation analysis, clustering, and functional enrichment. (**B** to **D**) Left panels: Identification of protein modules associated with sample traits in cytoplasm (B), nucleus (C), and EVs (D). Protein modules were identified and assigned distinct colors by the WGCNA algorithm to visually differentiate clusters of coexpressed proteins. Module-trait relationships were determined by bi-weight mid-correlation between module eigenprotein expression and sample traits, including infection, U6 snRNA, and EV count. Correlation coefficients (*r*) are indicated on the top with corresponding *P* values in brackets below. Positive correlations are highlighted in yellow, while negative correlations are in blue. Right panels: Enriched pathways of proteins in modules significantly correlated with infection ($r > 0.9$ or < -0.9, $P < 0.05$) in the cytoplasm (B), nucleus (C), and EVs (D). Positively correlated modules are highlighted in yellow, while negative correlations are shown in blue. Significantly enriched pathways by KEGG and STRING analysis (FDR < 0.05) are shown. (**E**) Protein number involved in nucleic acid processing pathways in cytoplasm, nucleus, and EVs. (**F**) Detected protein interaction modules involved in spliceosome pathway in nucleus and EVs.

DISCUSSION

On the basis of previous findings from the SIV-infected macaque model indicating increased levels of extracellular U6 snRNA in infection (*18*), we examined changes in U6 snRNA and associated proteins in cytoplasmic and nuclear cellular compartments as well as EVs of human immune cell lines infected with two virus strains. Decreased U6 snRNA in the nucleus corresponded with increased U6 in EVs, suggesting relocation and cellular export during infection.

U6 snRNA is a critical spliceosome component, primarily responsible for catalyzing the splicing of nuclear pre-mRNA (*33*). Its essential role in maintaining normal splicing processes has been demonstrated by studies showing that cellular U6 snRNA knockdown leads to increased intron retention for specific genes (*31*). Moreover, transient exogenous expression of U6 snRNA has been shown to slightly reduce mis-splicing rates of certain transcripts, further underscoring its role in regulating splicing fidelity (*34*). These findings suggest that reduced U6 snRNA levels within cells during infection could contribute to splicing dysregulation and altered gene expression patterns. In contrast, the observed increase of U6 in EVs raises important questions about its mechanism of incorporation, whether through selective sorting or as a consequence of infection-related cellular damage. Additionally, the potential functional impact of U6 snRNA in recipient cells remains unknown, highlighting the need for further investigations.

Protein profiling, in addition to revealing broad shifts across compartments and during infection, further suggested that U6 snRNA distribution changes are part of wider alterations in virus-induced splicing dysregulation. Aligned with previous studies, the proteome of EVs was notably different from that of intracellular compartments (*35*, *36*). Furthermore, the proteomes of EVs, the nucleus, and the cytoplasm were all distinctively altered in infected cells, consistent with previous reports on HIV infection (*37*, *38*). Several U6-related proteins were affected during infection, notably LSM8, essential for U6 snRNA nuclear localization (*39*), and SART3,

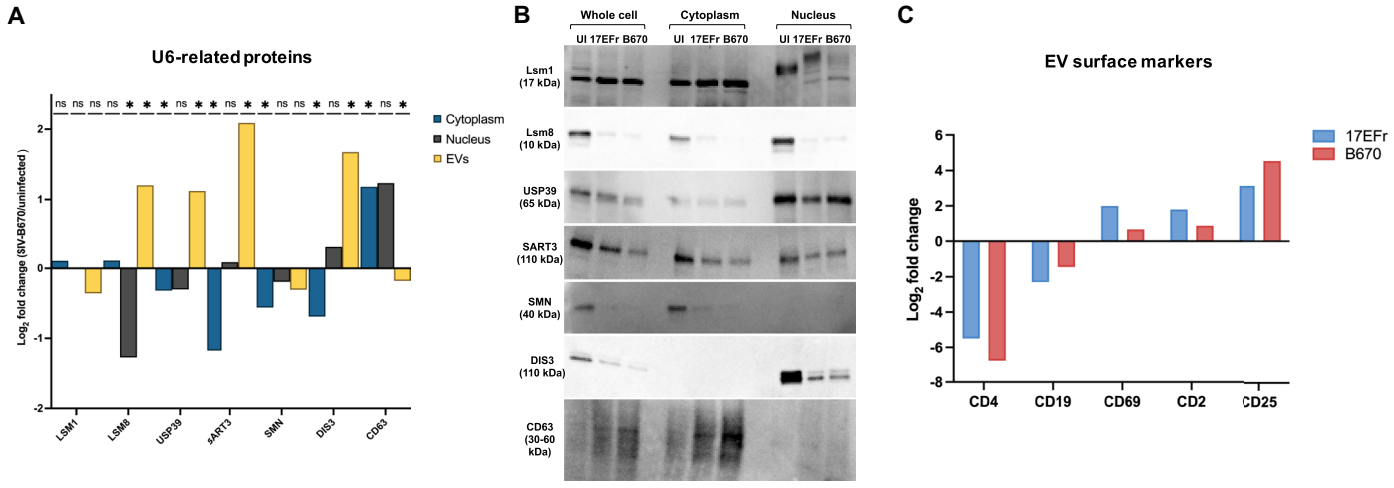

Fig. 5. U6 snRNA–associated proteins and EV surface markers in SIV infection. (**A**) Log_2 fold change of U6 snRNA–associated proteins between SIV-B670 infection and no infection in cytoplasm, nucleus, and EVs (proteomics). ns (no significant difference, $P > 0.05$), *adjusted P values < 0.05 (Benjamini-Hochberg method). (**B**) WBs of U6 snRNA–associated proteins in whole-cell, cytoplasm, and nucleus lysates; representative of three independent cell fractionation experiments. (**C**) Log_2 fold change of CD4, CD19, CD69, CD2, and CD25 (SIV-17EFr and SIV-B670 infection compared with uninfected controls) in EVs (MACSplex).

which forms an intermediate complex with U6 snRNA and is essential for spliceosome assembly (*40*). In addition, other key components of RNA processing and spliceosome were also altered during infection, such as USP39, a component protein of the U4/U6.U5 small nuclear ribonucleoprotein (snRNP) complex (*41*), and DIS3, which plays an important role in regulating the expression of specific spliceosome snRNAs (*42*). These findings underscore the notable impact of viral infection on U6 snRNA and broader RNA processing pathways.

In parallel, changes in U1 snRNA levels in the nucleus also reflect broader disruptions in RNA processing and spliceosome dynamics during infection. Both U1 and U6 snRNAs exhibited decreased nuclear levels; however, only U6 increased in EVs, suggesting distinct regulatory or sorting mechanisms. Previous studies have indicated tissue-dependent expression and regulation of snRNAs (*31*, *43*), and the recycling of snRNPs could affect their cellular reuse and differential release into EVs (*30*, *44*). Furthermore, variations in subtypes and levels of snRNA-associated proteins observed in the EV proteome, such as Prp24 and Lsm2-8 for U6, and SNRP70 for U1, may play a role in the selective packaging and transport of these snRNAs. To further explore these mechanisms, future studies should include investigations into RNA recycling and degradation pathways, and functional analyses of specific snRNP-associated proteins.

A question that arises from these results is whether they are due to general inflammatory or antiviral responses or are, instead, specific to retroviruses. While several studies have highlighted the impact of bacterial infections on the spliceosome and RNA splicing (*45*, *46*), research into how these components change during viral infections (*47*), especially in HIV (*47*, *48*), remains limited. While we cannot rule out general responses, the increases in EV U6 snRNA that we report here and in our previous study (*18*) do not hold for HBV-infected plasma EVs. Thus, at least some viral infections do not appear to produce the same shift in U6 distribution.

Possible effects of techniques and artifacts from CCM components should be carefully considered in evaluating results, especially when low-abundance materials like EV samples are involved. To be sure, our EV separation by size exclusion chromatography (SEC) has been previously validated (*49*), and we also rigorously evaluated the EV samples per MISEV guidelines (*1*, *2*). As recommended, we implemented MC. These controls revealed the presence of EVs, likely originating from FBS, that were characterized by high concentrations of FBS components. However, these EVs lacked detectable levels of cell-specific or typical EV markers, such as the tetraspanins CD63 and CD81. Additionally, both U6 and U1 snRNAs were significantly lower in these control samples, as indicated by the very high cycle of quantitation numbers in qPCR. Thus, although FBS contaminants were present, their consistency across the uninfected and infected groups, only trace amounts of measurable U6, supports the validity of our conclusions.

The relationship between host EVs and virions also bears discussion. The increase of U6 in EV-enriched fractions isolated by SEC was also found in EV subtypes as well as virion-enriched fractions that were further separated by density gradient ultracentrifugation (*18*). The difficulty of fully separating EVs from virions, due to their overlapping contents and physical characteristics, means that previous reports focusing on one category or the other may not be exclusive to either entity (*13*, *23*, *24*). Specifically, Pol III transcripts, including U6 snRNAs, were reported to be preferentially loaded into both EVs separated from uninfected cells (*50*) as well as virions that might be copurified with EVs in gradient-based isolation methods (*20*, *22*, *51*). This overlap aligns our findings with previous reports, demonstrating an increased transfer of U6 snRNA to extracellular compartments during infection, potentially affecting both EVs and virions. Notably, CD63, a common marker for both EVs and HIV (*52*, *53*), showed altered expression in our samples, reinforcing the connection between EVs and HIV. Packaging of snRNAs into retroviral virions can lead to snRNA reverse transcription and integration into the host genome (*21*). Potentially, EVs produced during infection might perform similar roles. Our findings highlight the complex interplay between EVs and virions in the context of HIV infection and potential shared contributions to RNA transfer and viral replication processes.

In summary, our research demonstrates a connection between EVs, U6 snRNA, RNA processing, and SIV infection. We characterized the increased packaging of nuclear proteins and RNAs into EVs or viral particles post-SIV infection. The changes observed in U6 snRNA and its associated proteins suggest that EVs play an important role in the dysfunctions and redirection of RNA processing that may be triggered by HIV infection. Future studies may include HIV-infected cell models and clinical samples, as well as examination of other retroviruses. Investigating the functions of U6 snRNA and its associated proteins in viral replication, particularly through the use of small-molecule inhibitors to disrupt SIV replication, could provide valuable insights into how viral replication influences host RNA processing. Additionally, exploring the mechanisms whereby EVs encapsulate RNA processing elements from the nucleus may provide deeper insights into the interaction between HIV and host cell RNA processing mechanisms.

MATERIALS AND METHODS

Cell culture

The B cell/T cell hybrid CEMx174 (gift from J. Hoxie, University of Pennsylvania) (*54*) was maintained in RPMI 1640 (Life Technologies) supplemented with 10% FBS (Atlanta Biologicals, Norcross, GA), 2 mM sodium pyruvate, 10 mM Hepes, gentamicin (0.5 mg/ml), and 2 mM L-glutamine (sR10 medium). H9 and PM1 (T lymphocytic lines) were obtained from AIDS Reagent and American Type Culture Collection (ATCC) and maintained in complete 10% FBS RPMI medium with 10 mM Hepes, 1 mM L-glutamine, and penicillin-streptomycin (1 mg/ml). Cells were grown at 37°C in a humidified 5% CO_2 incubator (*55*).

Virus stocks and infections

Simian immunodeficiency virus (SIV)/17EFr and Delta B670 virus swarms were prepared as previously described and stored at −80°C (*56*). The CEMx174 cells were counted by Muse Cell Analyzer (Millipore Corporation), washed one time in RPMI, and resuspended to 1×10^6 cells per well. SIV/17EFr and SIV/Delta B670 stocks were added separately to cells at 1×10^3 plaque-forming units (PFU) per well and incubated at 37°C for 72 hours. The infected CCM and cells were further split, incorporating uninfected cells to expand the infected culture. SIV infection was confirmed by cell syncytia formation, SIV p27 assay (ZeptoMetrix 0801169), and luciferase assay (*32*).

HIV-1 Rf and BAL stocks were generated from infected H9 and PM1 T lymphocytic cell lines, respectively, and stored at −80°C. HIV Rf or BAL stocks were added to H9 and PM1 cells at a concentration of 500 ng/ml (p24) and incubated at 37°C for 4 to 6 hours. Cells were then rinsed several times with phosphate-buffered saline (PBS) and spun twice at 400*g* for 5 min each (*55*).

Cell fractionation

Infected and uninfected cells (around 2×10^7) were washed twice with PBS and subsequently lysed in 2 ml of ice-cold 1% Triton in Dulbecco's PBS (DPBS) for 2 min. After pipetting up and down 10 times, 600 μl of the lysate was collected as whole-cell lysate. The remaining lysate was then subjected to centrifugation at 5000*g* for 5 min. The supernatant (cytosolic fraction) was collected (600 μl) and centrifuged again to eliminate any residual nuclei. The pelleted nuclear fraction was lysed once more in 1 ml of ice-cold 1% Triton. Following a 5000*g*, 5-min spin, supernatant was removed. To fully dissolve the nuclei, 600 μl 1% Triton was added to the pellets, followed by sonication in an ultrasonic ice bath at 20 kHz for three cycles of 2 min each, with a 30-s interval between each sonication.

EV separation

CCM (90 ml) from uninfected, SIV/17EFr-infected, and SIV/Delta B670–infected cells, as well as medium-only controls (MC), were collected and differentially centrifuged at 1000*g* for 10 min and 2000*g* for 15 min at 4°C. Supernatants were then transferred into 10-kDa protein concentrators (Millipore-Sigma, UFC701008) and concentrated to 10 ml. Retentate was then applied on the top of qEV10/70nm SEC columns (Izon Science, IC10-70) pre-rinsed with 150 ml of PBS. Fractions (5 ml) were collected by Izon automated fraction collectors (Izon Science). Fractions 1 to 4 (20 ml total) after the void volume (22.9 ml) were pooled as EV-enriched fractions and concentrated by 10-kDa molecular weight cutoff protein concentrators (Millipore-Sigma, UFC901008) to 550 μl. For EV separation from HBV-infected clinical plasma samples, see Supplementary Text.

Nanoflow cytometry

Concentration and size of EVs (1 μl, 1:1000 dilution) and MC (1 μl, 1:100 dilution) were measured for 1 min by side scatter using nanoflow cytometry (NFCM) calibrated for concentration and size with 200-nm silica beads and nanosphere mixture (diameters of 68, 91, 113, and 151 nm) as previously described (*57*).

Transmission electron microscopy

EV preparations and MC (8 μl, 1:2 diluted in DPBS) were absorbed onto glow-discharged 400-mesh ultrathin carbon-coated grids (EMS CF400-CU-UL) for 2 min, followed by three rinses in tris-buffered saline (TBS). Staining was performed using 1% uranyl acetate with 0.05% Tylose. After aspiration and drying, the grids were examined using a Philips CM120 instrument at 80 kV, and images were captured with an XR80 charge-coupled device (8 megapixels; AMT Imaging, Woburn, MA, USA).

Single-particle interferometric reflectance imaging sensor

SP-IRIS was performed as described (*57*). EVs and MC (1 μl) were diluted in 44 μl of incubation buffer (IB) and incubated overnight on ExoView tetraspanin chips (NanoView Biosciences). After 4 × 3 min washes in IB, chips were imaged (ExoView, NanoView) and analyzed (NanoViewer 2.8.10, NanoView).

EV analysis by bead-based multiplex flow cytometry assay (MACSplex)

EV fractions (5 μl) were subjected to bead-based multiplex analysis [Miltenyi, MACSPlex EV Kit IO (for immuno-oncology), 130-122-209] by flow cytometry (BD LSRFortessa). Thirty-seven EV surface epitopes plus two isotype controls were tested according to the manufacturer's protocol. The average APC medians of individual bead populations were used to determine the expression of EV surface markers.

Total RNA extraction

RNA was extracted from 250 μl each of EVs and MC with TRIzol LS (Thermo Fisher Scientific, 10296028), and 200 μl each of whole-cell lysates, cytoplasm, and nucleus using TRIzol (Thermo Fisher Scientific, 15596018). After homogenization, RNA was isolated by miRNeasy solutions (Qiagen, 217004) with Zymo-Spin columns (Zymo

Research, C1003–50) per the manufacturer's instruction. The concentration of extracted RNA was measured using a NanoDrop spectrophotometer. To ensure consistency across samples, the RNA concentration was adjusted to be equivalent within the uninfected, SIV-17EFr, and SIV-B670 groups within each experimental batch.

Individual quantitative PCR assays

qPCR assays were performed using equal amounts of RNAs within each batch for U6 snRNA using TaqMan MicroRNA Assays (Thermo Fisher Scientific, Assay ID 001973) and miRCURY LNA miRNA PCR Assay (Qiagen, GeneGlobe ID YP00203907). qPCR assays for U1 snRNA were performed by miRCURY LNA miRNA PCR Assay (Qiagen, Assay GeneGlobe ID YP00203909).

Fluorescence imaging

The U6 snRNA sequence was retrieved from the National Center for Biotechnology Information (NCBI) Reference Sequence Database (RefSeq accession number NR_004394.1). Five probes targeting regions across the U6 snRNA sequence (atgtgctgccgaagcgagc, gtatcgttccaattttagt, ggggccatgctaatcttct, tttgcgtgtcatccttgcg, aaatatggaacgcttcacg) were designed using Stellaris Probe Designer (Biosearch Technologies). Each probe was synthesized with a 3′ amino modification to facilitate conjugation. The probes were pooled in equimolar concentrations and conjugated with Texas Red (TR) fluorophore (Invitrogen, T6134) followed by high-pressure liquid chromatography (HPLC) purification as previously described (*58*). CEM174 cells were fixed using 4% formaldehyde and subsequently stored in 70% ethanol at 4°C. Before hybridization, cells were washed with a buffer containing 2× saline sodium citrate (SSC) solution (Ambion, AM9763), 20% formamide (Ambion, AM9342), and 2 mM ribonucleoside vanadyl complex (New England Biolabs, S1402S). Hybridization was performed by incubating the cells with U6 snRNA probe sets (25 ng/μl) diluted in 100 μl of hybridization buffer [containing 10% dextran sulfate (Sigma, D8906), yeast tRNA (1 μg/μl; Invitrogen, 15401-029), 2 mM ribonucleoside-vanadyl complex, 0.02% ribonuclease-free bovine serum albumin (BSA) (Ambion, AM2618), and 20% formamide dissolved in 2× SSC] on coverslips in a humidified chamber overnight at 37°C. Post-hybridization, cells attached to coverslips were washed and stained with DAPI to visualize nuclear DNA (Sigma, D9542). The prepared samples were then mounted using established protocols (*59*). The images were taken with 40×/1.30 PlanNeofluar oil objective on a Zeiss LSM 800 Confocal Laser Scanning Microscope. Initial overview images were acquired at ×20 magnification, followed by high-resolution z-stack imaging at ×40 across four to five distinct positions per slide. The acquired images were analyzed using Imaris software to assess colocalization. The "Colocalization" tool in Imaris was used to identify and count voxels, where TR and DAPI signals overlap. The number of colocalized voxels was quantified, and the percentage of colocalized voxels relative to the total number of voxels in the defined cell area (Colocalization %) was calculated and presented.

Mass spectrometry

Sample preparation, protein digestion, and peptide TMT labeling

Cytoplasm and nucleus samples were resuspended in 1× radioimmunoprecipitation assay (RIPA) (Cell Signaling Technology) with protease inhibitors and incubated on ice for 5 min. The samples were sonicated for 5 min in the ice water bath before centrifugation at 14,000*g* at 4°C for 15 min. The supernatant was then collected as lysed proteins. EVs and MC were resuspended in DPBS and lysed with 0.05% SDS. Protein concentration was assessed by bicinchoninic acid assay (BCA) assay (Thermo Fisher Scientific, 23250). Proteins (50 μg) of cytoplasm, nucleus, and EVs samples, as well as 30 μg of MC samples, were dried in a speed vacuum and reconstituted in triethylammonium bicarbonate (TEAB) buffer. Samples were then treated with dithiothreitol (DTT) and iodoacetamide for reduction and alkylation. SP3 beads were used for protein purification, followed by overnight digestion with trypsin at 37°C directly on the beads. Post-digestion, peptides were labeled with TMT10plex isobaric label reagent for quantitative analysis.

Liquid chromatography separation and tandem mass spectrometry

For peptide fractionation, the tandem mass tag (TMT)-labeled peptides were reconstituted, cleaned to remove any excess labels, lipids, and small molecules, and subjected to basic reversed-phase chromatography using an Agilent HPLC system. This process involved an 85-min gradient to separate peptides, transitioning from 100% solvent A (10 mM TEAB in water) to 100% solvent B (90% acetonitrile/10 mM TEAB). Fractionated peptides were then analyzed on a nano-LC-Orbitrap system. The system used a reversed-phase chromatography gradient from 2% to 90% acetonitrile in 0.1% formic acid over 82 min. Eluted peptides were sprayed into an Orbitrap-Fusion-LumosIC mass spectrometer through a 1-μm emitter tip (New Objective) at 2.4 kV. Initial survey scans (full MS) were acquired in the Orbitrap analyzer within a mass-to-charge (m/z) range of 375 to 1600. Top 15 most intense ions from the survey scan were selected for further analysis, using a dynamic exclusion duration of 15 s. Precursor ions were individually isolated with a window of 0.7 Da, fragmented (MS/MS) using a higher-energy collisional dissociation (HCD) with a set collision energy of 40. Precursor (MS1) and fragment (MS2) ions were subsequently analyzed at a resolution of 120,000 and 50,000, respectively.

MS data processing and analysis

Tandem MS2 spectra (signal/noise > 2) were processed by Proteome Discoverer (v2.4, Thermo Fisher Scientific) using the Files RC option. MS/MS spectra were searched with Mascot v. 2.8.0 (Matrix Science, London, UK) against RefSeq2021_204_Human database and a small database containing enzymes, BSA. Trypsin specificity was used for the digestion, with up to two missed cleavages. Methionine oxidation and deamidation were selected as the variable modifications. Carbamidomethylation of cysteines and TMT-label modifications of N termini and lysine were set as fixed modifications. Peptide identifications from the Mascot searches were processed within the Proteome Discoverer and Percolator to identify peptides with a confidence threshold of 1% false discovery rate (FDR). Only top ranked (rank 1) peptides were considered. Quantitative analyses were normalized across all identified peptides, while quantification ratios were computed exclusively from unique peptides. Quality control thresholds were applied, requiring a reporter signal-to-noise ratio (SN) > 5 and isolation interference < 25%. Protein identifications were classified into high, medium, or low confidence levels based on the Percolator, with inclusion criteria requiring at least one high-confidence peptide (1% FDR, rank 1) per protein.

The threshold for significant differential abundance of proteins was defined at adjusted P values <0.05 (Benjamini-Hochberg

method), as calculated using a non-nested analysis of variance (ANOVA) test per Proteome Discoverer 2.4 recommendations. Nonscaled proteomics data were visualized with a PCA plot. The protein interaction, protein cluster function prediction, cellular component, and biological process annotations were done by Protein-Protein Interaction Networks Functional Enrichment Analysis (STRING) in Cytoscape (*60*). Venn diagrams were generated in R by VennDiagram and UpSetR packages.

Weighted gene coexpression network analysis (WGCNA)

WGCNA R package (*61*) was carried out to establish protein correlation modules for DE proteins identified in both 17EFr- and B670-infected samples compared with uninfected samples, across cytoplasm, nucleus, and EVs (Fig. 4A). Briefly, gene coexpression networks were constructed based on a correlation matrix of protein levels in all samples. The matrix was then subjected to specific module cutting parameters (power = the optimal power defined by pickSoftThreshold, minimum module size = 30, deepSplit = 3, threshold of correlation = 0.01) to define protein modules based on hierarchical clustering. Protein modules with distinct coexpression patterns were assigned unique color labels by the software. These arbitrary colors aid in visually distinguishing each module in network plots and facilitate subsequent functional enrichment annotations. The eigengene network was then constructed to calculate the correlation of protein modules to sample traits. PPI networks and function enrichment analysis of significantly correlated modules were predicted using STRING in Cytoscape (*60*).

Western blotting

Whole-cell lysates, cytosolic fractions, nuclear fractions, and EVs were lysed in 1× RIPA buffer (Cell Signaling Technology, 9806). Protein concentrations were determined by BCA protein assay (Thermo Fisher Scientific, 23250). Equivalent amounts of total protein from cellular samples and equivalent volumes from EV samples were separated on 4 to 15% stain-free SDS–polyacrylamide gel electrophoresis (PAGE) gradient gels (Bio-Rad, 5678083) under nonreducing conditions and transferred onto polyvinylidene difluoride (PVDF) membranes (Sigma-Aldrich, IPVH00010). After 1-hour blocking in 5% nonfat milk solution (Bio-Rad, 170–6404), membranes were incubated with anti-SMN (1:2000 dilution), anti-CD63 (1:500 dilution) (BD Biosciences, 610646 and 556019, respectively), anti–lamin B1 (1:1000), anti-GAPDH (1:1000) (Abcam, ab16048, ab8245), anti-tubulin (1:1000, Novus Biologicals, NB100-690), anti-LSM1 (1:1000, LSBio, LS-C97364-400), anti-LSM8 (1:200, Santa Cruz Biotechnology, sc-81315), anti-SART3 (1:2000), anti-DIS3 (1:500), and anti-USP39 (1:500) (Proteintech, 18025-1-AP, 14689-1-AP, 23865-1-AP) overnight at 4°C. The membrane was then incubated with horseradish peroxidase (HRP)–conjugated secondary antibody (1:10,000 dilution) (Santa Cruz Biotechnology, sc-2357, sc-516102) at room temperature for 1 hour after washing in PBST. After washing in PBST again, SuperSignal West Pico PLUS Chemiluminescent Substrate (Thermo Fisher Scientific, 34580) was applied, and blots were visualized using a Thermo Fisher Scientific iBright 1500 imaging system.

Statistical analysis, data availability, and EV-TRACK

The statistical significance of differences was assessed variously by ANOVA, Tukey's multiple comparisons test, and unpaired *t* test, as indicated in figure legends for individual tests. Proteomics data files are available on request. We have submitted all relevant data of our experiments to the EV-TRACK knowledgebase (EV-TRACK ID: EV240032) (*62*).

Supplementary Materials

This PDF file includes:

Supplementary Text
Figs. S1 to S7
Table S1

REFERENCES AND NOTES

1. J. A. Welsh, D. C. I. Goberdhan, L. O'Driscoll, E. I. Buzas, C. Blenkiron, B. Bussolati, H. Cai, D. Di Vizio, T. A. P. Driedonks, U. Erdbrugger, J. M. Falcon-Perez, Q. L. Fu, A. F. Hill, M. Lenassi, S. K. Lim, M. G. Mahoney, S. Mohanty, A. Moller, R. Nieuwland, T. Ochiya, S. Sahoo, A. C. Torrecilhas, L. Zheng, A. Zijlstra, S. Abuelreich, R. Bagabas, P. Bergese, E. M. Bridges, M. Brucale, D. Burger, R. P. Carney, E. Cocucci, R. Crescitelli, E. Hanser, A. L. Harris, N. J. Haughey, A. Hendrix, A. R. Ivanov, T. Jovanovic-Talisman, N. A. Kruh-Garcia, V. Ku'ulei-Lyn Faustino, D. Kyburz, C. Lasser, K. M. Lennon, J. Lotvall, A. L. Maddox, E. S. Martens-Uzunova, R. R. Mizenko, L. A. Newman, A. Ridolfi, E. Rohde, T. Rojalin, A. Rowland, A. Saftics, U. S. Sandau, J. A. Saugstad, F. Shekari, S. Swift, D. Ter-Ovanesyan, J. P. Tosar, Z. Useckaite, F. Valle, Z. Varga, E. van der Pol, M. J. C. van Herwijnen, M. H. M. Wauben, A. M. Wehman, S. Williams, A. Zendrini, A. J. Zimmerman, MISEV Consortium, C. Thery, K. W. Witwer, Minimal information for studies of extracellular vesicles (MISEV2023): From basic to advanced approaches. *J. Extracell. Vesicles* **13**, e12404 (2024).
2. C. Théry, K. W. Witwer, E. Aikawa, M. J. Alcaraz, J. D. Anderson, R. Andriantsitohaina, A. Antoniou, T. Arab, F. Archer, G. K. Atkin-Smith, D. C. Ayre, J.-M. Bach, D. Bachurski, H. Baharvand, L. Balaj, S. Baldacchino, N. N. Bauer, A. A. Baxter, M. Bebawy, C. Beckham, A. B. Zavec, A. Benmoussa, A. C. Berardi, P. Bergese, E. Bielska, C. Blenkiron, S. Bobis-Wozowicz, E. Boilard, W. Boireau, A. Bongiovanni, F. E. Borràs, S. Bosch, C. M. Boulanger, X. Breakefield, A. M. Breglio, M. Á. Brennan, D. R. Brigstock, A. Brisson, M. L. Broekman, J. F. Bromberg, P. Bryl-Górecka, S. Buch, A. H. Buck, D. Burger, S. Busatto, D. Buschmann, B. Bussolati, E. I. Buzás, J. B. Byrd, G. Camussi, D. R. Carter, S. Caruso, L. W. Chamley, Y.-T. Chang, C. Chen, S. Chen, L. Cheng, A. R. Chin, A. Clayton, S. P. Clerici, A. Cocks, E. Cocucci, R. J. Coffey, A. Cordeiro-da-Silva, Y. Couch, F. A. Coumans, B. Coyle, R. Crescitelli, M. F. Criado, C. D'Souza-Schorey, S. Das, A. D. Chaudhuri, P. de Candia, E. F. De Santana, O. De Wever, H. A. Del Portillo, T. Demaret, S. Deville, A. Devitt, B. Dhondt, D. D. Vizio, L. C. Dieterich, V. Dolo, A. P. D. Rubio, M. Dominici, M. R. Dourado, T. A. Driedonks, F. V. Duarte, H. M. Duncan, R. M. Eichenberger, K. Ekström, S. E. Andaloussi, C. Elie-Caille, U. Erdbrügger, J. M. Falcón-Pérez, F. Fatima, J. E. Fish, M. Flores-Bellver, A. Försönits, A. Frelet-Barrand, F. Fricke, G. Fuhrmann, S. Gabrielsson, A. Gámez-Valero, C. Gardiner, K. Gärtner, R. Gaudin, Y. S. Gho, B. Giebel, C. Gilbert, M. Gimona, I. Giusti, D. C. Goberdhan, A. Görgens, S. M. Gorski, D. W. Greening, J. C. Gross, A. Gualerzi, G. N. Gupta, D. Gustafson, A. Handberg, R. A. Haraszti, P. Harrison, H. Hegyesi, A. Hendrix, A. F. Hill, F. H. Hochberg, K. F. Hoffmann, B. Holder, H. Holthofer, B. Hosseinkhani, G. Hu, Y. Huang, V. Huber, S. Hunt, A. G.-E. Ibrahim, T. Ikezu, J. M. Inal, M. Isin, A. Ivanova, H. K. Jackson, S. Jacobsen, S. M. Jay, M. Jayachandran, G. Jenster, L. Jiang, S. M. Johnson, J. C. Jones, A. Jong, T. Jovanovic-Talisman, S. Jung, R. Kalluri, S.-I. Kano, S. Kaur, Y. Kawamura, E. T. Keller, D. Khamari, E. Khomyakova, A. Khvorova, P. Kierulf, K. P. Kim, T. Kislinger, M. Klingeborn, D. J. Klinke II, M. Kornek, M. M. Kosanović, Á. F. Kovács, E.-M. Krämer-Albers, S. Krasemann, M. Krause, I. V. Kurochkin, G. D. Kusuma, S. Kuypers, S. Laitinen, S. M. Langevin, L. R. Languino, J. Lannigan, C. Lässer, L. C. Laurent, G. Lavieu, E. Lázaro-Ibáñez, S. L. Lay, M.-S. Lee, Y. X. F. Lee, D. S. Lemos, M. Lenassi, A. Leszczynska, I. T. Li, K. Liao, S. F. Libregts, E. Ligeti, R. Lim, S. K. Lim, A. Linē, K. Linnemannstöns, A. Llorente, C. A. Lombard, M. J. Lorenowicz, Á. M. Lörincz, J. Lötvall, J. Lovett, M. C. Lowry, X. Loyer, Q. Lu, B. Lukomska, T. R. Lunavat, S. L. Maas, H. Malhi, A. Marcilla, J. Mariani, J. Mariscal, E. S. Martens-Uzunova, L. Martin-Jaular, M. C. Martinez, V. R. Martins, M. Mathieu, S. Mathivanan, M. Maugeri, L. K. M. Ginnis, M. J. M. Vey, D. G. Meckes Jr., K. L. Meehan, I. Mertens, V. R. Minciacchi, A. Möller, M. M. Jørgensen, A. Morales-Kastresana, J. Morhayim, F. Mullier, M. Muraca, L. Musante, V. Mussack, D. C. Muth, K. H. Myburgh, T. Najrana, M. Nawaz, I. Nazarenko, P. Nejsum, C. Neri, T. Neri, R. Nieuwland, L. Nimrichter, J. P. Nolan, E. N. N. -'t Hoen, N. N. Hooten, L. O. 'Driscoll, T. O. 'Grady, A. O. 'Loghlen, T. Ochiya, M. Olivier, A. Ortiz, L. A. Ortiz, X. Osteikoetxea, O. Østergaard, M. Ostrowski, J. Park, D. M. Pegtel, H. Peinado, F. Perut, M. W. Pfaffl, D. G. Phinney, B. C. Pieters, R. C. Pink, D. S. Pisetsky, E. P. von Strandmann, I. Polakovicova, I. K. Poon, B. H. Powell, I. Prada, L. Pulliam, P. Quesenberry, A. Radeghieri, R. L. Raffai, S. Raimondo, J. Rak, M. I. Ramirez, G. Raposo, M. S. Rayyan, N. Regev-Rudzki, F. L. Ricklefs, P. D. Robbins, D. D. Roberts, S. C. Rodrigues, E. Rohde, S. Rome, K. M. Rouschop, A. Rughetti, A. E. Russell, P. Saá, S. Sahoo, E. Salas-Huenuleo, C. Sánchez, J. A. Saugstad,

M. J. Saul, R. M. Schiffelers, R. Schneider, T. H. Schøyen, A. Scott, E. Shahaj, S. Sharma, O. Shatnyeva, F. Shekari, G. V. Shelke, A. K. Shetty, K. Shiba, P. R.-M. Siljander, A. M. Silva, A. Skowronek, O. L. Snyder II, R. P. Soares, B. W. Sódar, C. Soekmadji, J. Sotillo, P. D. Stahl, W. Stoorvogel, S. L. Stott, E. F. Strasser, S. Swift, H. Tahara, M. Tewari, K. Timms, S. Tiwari, R. Tixeira, M. Tkach, W. S. Toh, R. Tomasini, A. C. Torrecilhas, J. P. Tosar, V. Toxavidis, L. Urbanelli, P. Vader, B. W. van Balkom, S. G. van der Grein, J. Van Deun, M. J. van Herwijnen, K. Van Keuren-Jensen, G. van Niel, M. E. van Royen, A. J. van Wijnen, M. H. Vasconcelos, I. J. Vechetti Jr., T. D. Veit, L. J. Vella, É. Velot, F. J. Verweij, B. Vestad, J. L. Viñas, T. Visnovitz, K. V. Vukman, J. Wahlgren, D. C. Watson, M. H. Wauben, A. Weaver, J. P. Webber, V. Weber, A. M. Wehman, D. J. Weiss, J. A. Welsh, S. Wendt, A. M. Wheelock, Z. Wiener, L. Witte, J. Wolfram, A. Xagorari, P. Xander, J. Xu, X. Yan, M. Yáñez-Mó, H. Yin, Y. Yuana, V. Zappulli, J. Zarubova, V. Žėkas, J.-Y. Zhang, Z. Zhao, L. Zheng, A. R. Zheutlin, A. M. Zickler, P. Zimmermann, A. M. Zivkovic, D. Zocco, E. K. Zuba-Surma, Minimal information for studies of extracellular vesicles 2018 (MISEV2018): A position statement of the International Society for Extracellular Vesicles and update of the MISEV2014 guidelines. *J. Extracell. Vesicles* **7**, 1535750–1532018 (2018).
3. M. Stenovec, E. Lasič, P. P. Dominkus, S. T. Bobnar, R. Zorec, M. Lenassi, M. Kreft, Slow release of HIV-1 protein Nef from vesicle-like structures is inhibited by cytosolic calcium elevation in single human microglia. *Mol. Neurobiol.* **56**, 102–118 (2019).
4. A. M. Booth, Y. Fang, J. K. Fallon, J. M. Yang, J. E. Hildreth, S. J. Gould, Exosomes and HIV Gag bud from endosome-like domains of the T cell plasma membrane. *J. Cell Biol.* **172**, 923–935 (2006).
5. M. N. Madison, C. M. Okeoma, Exosomes: Implications in HIV-1 Pathogenesis. *Viruses* **7**, 4093–4118 (2015).
6. S. Biswas, M. Haleyurgirisetty, V. Ragupathy, X. Wang, S. Lee, I. Hewlett, K. Devadas, Differentially expressed host long intergenic noncoding RNA and mRNA in HIV-1 and HIV-2 infection. *Sci. Rep.* **8**, 2546 (2018).
7. M. Lu, W. Shao, H. Xing, Y. Huang, Extracellular vesicle-based nucleic acid delivery. *Interdiscip. Med.* **1**, e20220007 (2023).
8. G. Sun, H. Li, X. Wu, M. Covarrubias, L. Scherer, K. Meinking, B. Luk, P. Chomchan, J. Alluin, A. F. Gombart, J. J. Rossi, Interplay between HIV-1 infection and host microRNAs. *Nucleic Acids Res.* **40**, 2181–2196 (2012).
9. A. Turchinovich, L. Weiz, A. Langheinz, B. Burwinkel, Characterization of extracellular circulating microRNA. *Nucleic Acids Res.* **39**, 7223–7233 (2011).
10. Y. Huang, T. Arab, A. E. Russell, E. R. Mallick, R. Nagaraj, E. Gizzie, J. Redding-Ochoa, J. C. Troncoso, O. Pletnikova, A. Turchinovich, D. A. Routenberg, K. W. Witwer, Toward a human brain extracellular vesicle atlas: Characteristics of extracellular vesicles from different brain regions, including small RNA and protein profiles. *Interdiscip. Med.* **1**, e20230016 (2023).
11. J. P. Tosar, F. Gámbaro, J. Sanguinetti, B. Bonilla, K. W. Witwer, A. Cayota, Assessment of small RNA sorting into different extracellular fractions revealed by high-throughput sequencing of breast cell lines. *Nucleic Acids Res.* **43**, 5601–5616 (2015).
12. E. Poveda, M. L. Freeman, Exosomes as new players in HIV pathogenesis—New data from the IAS 2017. *AIDS Rev.* **19**, 173–175 (2017).
13. P. S. Pérez, M. A. Romaniuk, G. A. Duette, Z. Zhao, Y. Huang, L. Martin-Jaular, K. W. Witwer, C. Théry, M. Ostrowski, Extracellular vesicles and chronic inflammation during HIV infection. *J. Extracell. Vesicles* **8**, 1687275 (2019).
14. Y. Huang, A. Abdelgawad, A. Turchinovich, S. Queen, C. M. Abreu, X. Zhu, M. Batish, L. Zheng, K. W. Witwer, RNA landscapes of brain and brain-derived extracellular vesicles in simian immunodeficiency virus (SIV) infection and central nervous system pathology. *J. Infect. Dis.* **229**, 1295–1305 (2023).
15. W. S. Hu, S. H. Hughes, HIV-1 reverse transcription. *Cold Spring Harb. Perspect. Med.* **2**, a006882 (2012).
16. P. J. Tomezsko, V. D. A. Corbin, P. Gupta, H. Swaminathan, M. Glasgow, S. Persad, M. D. Edwards, L. McIntosh, A. T. Papenfuss, A. Emery, R. Swanstrom, T. Zang, T. C. T. Lan, P. Bieniasz, D. R. Kuritzkes, A. Tsibris, S. Rouskin, Determination of RNA structural diversity and its role in HIV-1 RNA splicing. *Nature* **582**, 438–442 (2020).
17. X. Lu, J. Yang, H. Wu, Z. Yang, C. Jin, J. Wang, L. Cheng, X. Peng, F. Liu, X. Peng, S. Ji, H. Ou, T. Xie, H. Yao, N. Wu, High-throughput sequencing identifies HIV-1-replication- and latency-related miRNAs in $CD4^+$ T cell lines. *Arch. Virol.* **162**, 1933–1942 (2017).
18. Y. Huang, Z. Liao, P. Dang, S. Queen, C. M. Abreu, O. Gololobova, L. Zheng, K. W. Witwer, Longitudinal characterization of circulating extracellular vesicles and small RNA during simian immunodeficiency virus infection and antiretroviral therapy. *AIDS* **37**, 733–744 (2023).
19. S. Chettimada, D. R. Lorenz, V. Misra, S. M. Wolinsky, D. Gabuzda, Small RNA sequencing of extracellular vesicles identifies circulating miRNAs related to inflammation and oxidative stress in HIV patients. *BMC Immunol.* **21**, 57 (2020).
20. L. Didierlaurent, P. J. Racine, L. Houzet, C. Chamontin, B. Berkhout, M. Mougel, Role of HIV-1 RNA and protein determinants for the selective packaging of spliced and unspliced viral RNA and host U6 and 7SL RNA in virus particles. *Nucleic Acids Res.* **39**, 8915–8927 (2011).
21. K. E. Giles, M. Caputi, K. L. Beemon, Packaging and reverse transcription of snRNAs by retroviruses may generate pseudogenes. *RNA* **10**, 299–307 (2004).
22. C. Tian, T. Wang, W. Zhang, X. F. Yu, Virion packaging determinants and reverse transcription of SRP RNA in HIV-1 particles. *Nucleic Acids Res.* **35**, 7288–7302 (2007).
23. E. Nolte-'t Hoen, T. Cremer, R. C. Gallo, L. B. Margolis, Extracellular vesicles and viruses: Are they close relatives? *Proc. Natl. Acad. Sci. U.S.A.* **113**, 9155–9161 (2016).
24. R. P. McNamara, D. P. Dittmer, Modern techniques for the isolation of extracellular vesicles and viruses. *J. Neuroimmune Pharmacol.* **15**, 459–472 (2020).
25. M. Puigdelloses, M. González-Huárriz, M. García-Moure, N. Martínez-Vélez, I. E. Vázquez, J. Bruna, B. Zandio, A. Agirre, M. Marigil, G. Petrirena, J. M. Nuñez-Córdoba, S. Tejada-Solís, R. Díez-Valle, J. Gállego-Culleré, E. Martínez-Vila, A. Patiño-García, M. M. Alonso, J. G. Pérez-Larraya, RNU6-1 in circulating exosomes differentiates GBM from non-neoplastic brain lesions and PCNSL but not from brain metastases. *Neurooncol. Adv.* **2**, vdaa010 (2020).
26. L. Manterola, E. Guruceaga, J. G. Pérez-Larraya, M. González-Huarriz, P. Jauregui, S. Tejada, R. Diez-Valle, V. Segura, N. Samprón, C. Barrena, I. Ruiz, A. Agirre, A. Ayuso, J. Rodríguez, A. González, E. Xipell, A. Matheu, A. L. de Munain, T. Tuñón, I. Zazpe, J. García-Foncillas, S. Paris, J. Y. Delattre, M. M. Alonso, A small noncoding RNA signature found in exosomes of GBM patient serum as a diagnostic tool. *Neuro Oncol.* **16**, 520–527 (2014).
27. K. Chiam, T. Wang, D. I. Watson, G. C. Mayne, T. S. Irvine, T. Bright, L. Smith, I. A. White, J. M. Bowen, D. Keefe, S. K. Thompson, M. E. Jones, D. J. Hussey, Circulating serum exosomal miRNAs as potential biomarkers for esophageal adenocarcinoma. *J. Gastrointest. Surg.* **19**, 1208–1215 (2015).
28. G. W. Zieve, R. A. Sauterer, R. J. Feeney, Newly synthesized small nuclear RNAs appear transiently in the cytoplasm. *J. Mol. Biol.* **199**, 259–267 (1988).
29. J. L. Liu, J. G. Gall, U bodies are cytoplasmic structures that contain uridine-rich small nuclear ribonucleoproteins and associate with P bodies. *Proc. Natl. Acad. Sci. U.S.A.* **104**, 11655–11659 (2007).
30. A. L. Didychuk, S. E. Butcher, D. A. Brow, The life of U6 small nuclear RNA, from cradle to grave. *RNA* **24**, 437–460 (2018).
31. H. Dvinge, J. Guenthoer, P. L. Porter, R. K. Bradley, RNA components of the spliceosome regulate tissue- and cancer-specific alternative splicing. *Genome Res.* **29**, 1591–1604 (2019).
32. J. W. Roos, M. F. Maughan, Z. Liao, J. E. Hildreth, J. E. Clements, LuSIV cells: A reporter cell line for the detection and quantitation of a single cycle of HIV and SIV replication. *Virology* **273**, 307–315 (2000).
33. S. M. Fica, N. Tuttle, T. Novak, N. S. Li, J. Lu, P. Koodathingal, Q. Dai, J. P. Staley, J. A. Piccirilli, RNA catalyses nuclear pre-mRNA splicing. *Nature* **503**, 229–234 (2013).
34. M. Yahara, A. Kitamura, M. Kinjo, U6 snRNA expression prevents toxicity in TDP-43-knockdown cells. *PLOS ONE* **12**, e0187813 (2017).
35. D. W. Greening, R. Xu, S. K. Gopal, A. Rai, R. J. Simpson, Proteomic insights into extracellular vesicle biology - defining exosomes and shed microvesicles. *Expert Rev. Proteomics* **14**, 69–95 (2017).
36. R. A. Haraszti, M.-C. Didiot, E. Sapp, J. Leszyk, S. A. Shaffer, H. E. Rockwell, F. Gao, N. R. Narain, M. DiFiglia, M. A. Kiebish, N. Aronin, A. Khvorova, High-resolution proteomic and lipidomic analysis of exosomes and microvesicles from different cell sources. *J. Extracell. Vesicles* **5**, 32570 (2016).
37. L. Martin-Jaular, N. Nevo, J. P. Schessner, M. Tkach, M. Jouve, F. Dingli, D. Loew, K. W. Witwer, M. Ostrowski, G. H. H. Borner, C. Théry, Unbiased proteomic profiling of host cell extracellular vesicle composition and dynamics upon HIV-1 infection. *EMBO J.* **40**, e105492 (2021).
38. S. Moron-Lopez, S. Telwatte, I. Sarabia, E. Battivelli, M. Montano, A. B. Macedo, D. Aran, A. J. Butte, R. B. Jones, A. Bosque, E. Verdin, W. C. Greene, J. K. Wong, S. A. Yukl, Human splice factors contribute to latent HIV infection in primary cell models and blood $CD4^+$ T cells from ART-treated individuals. *PLOS Pathog.* **16**, e1009060 (2020).
39. M. P. Spiller, K.-L. Boon, M. A. Reijns, J. D. Beggs, The Lsm2-8 complex determines nuclear localization of the spliceosomal U6 snRNA. *Nucleic Acids Res.* **35**, 923–929 (2007).
40. D. Staněk, S. D. Rader, M. Klingauf, K. M. Neugebauer, Targeting of U4/U6 small nuclear RNP assembly factor SART3/p110 to Cajal bodies. *J. Cell Biol.* **160**, 505–516 (2003).
41. G. X. Ruan, Y. Li, W. Chen, H. Huang, R. Zhang, C. Chen, K. P. Lam, S. Xu, X. Ou, The spliceosome component Usp39 controls B cell development by regulating immunoglobulin gene rearrangement. *Cell Rep.* **38**, 110338 (2022).
42. C. Kilchert, S. Wittmann, L. Vasiljeva, The regulation and functions of the nuclear RNA exosome complex. *Nat. Rev. Mol. Cell Biol.* **17**, 227–239 (2016).
43. K. Fukumura, I. Taniguchi, H. Sakamoto, M. Ohno, K. Inoue, U1-independent pre-mRNA splicing contributes to the regulation of alternative splicing. *Nucleic Acids Res.* **37**, 1907–1914 (2009).
44. Y. Shi, Mechanistic insights into precursor messenger RNA splicing by the spliceosome. *Nat. Rev. Mol. Cell Biol.* **18**, 655–670 (2017).
45. J. Tsalikis, I. Tattoli, A. Ling, M. T. Sorbara, D. O. Croitoru, D. J. Philpott, S. E. Girardin, Intracellular bacterial pathogens trigger the formation of U small nuclear RNA bodies (U bodies) through metabolic stress induction. *J. Biol. Chem.* **290**, 20904–20918 (2015).
46. H. Kalam, M. F. Fontana, D. Kumar, Alternate splicing of transcripts shape macrophage response to Mycobacterium tuberculosis infection. *PLOS Pathog.* **13**, e1006236 (2017).

47. D. R. Ram, K. Kroll, R. K. Reeves, Skipped over: Tuning natural killer cells toward HIV through alternative splicing. *AIDS Res. Hum. Retroviruses* **36**, 969–972 (2020).
48. F. Kadri, M. Pacifici, A. Wilk, A. Parker-Struckhoff, L. Del Valle, K. F. Hauser, P. E. Knapp, C. Parsons, D. Jeansonne, A. Lassak, F. Peruzzi, HIV-1-Tat protein inhibits SC_{35}-mediated tau exon 10 inclusion through up-regulation of DYRK1A kinase. *J. Biol. Chem.* **290**, 30931–30946 (2015).
49. B. V. Rodriguez, Y. Wen, E. N. Shirk, S. Vazquez, O. Gololobova, A. Maxwell, J. Plunkard, N. Castell, B. Carlson, S. E. Queen, J. M. Izzi, T. A. P. Driedonks, K. W. Witwer, An ex vivo model of interactions between extracellular vesicles and peripheral mononuclear blood cells in whole blood. *J. Extracell. Vesicles* **12**, e12368 (2023).
50. M. L. Mosbach, C. Pfafenrot, E. P. von Strandmann, A. Bindereif, C. Preusser, Molecular determinants for RNA release into extracellular vesicles. *Cells* **10**, 2674 (2021).
51. A. A. Onafuwa-Nuga, S. R. King, A. Telesnitsky, Nonrandom packaging of host RNAs in moloney murine leukemia virus. *J. Virol.* **79**, 13528–13537 (2005).
52. E. Fu, L. Pan, Y. Xie, D. Mu, W. Liu, F. Jin, X. Bai, Tetraspanin CD63 is a regulator of HIV-1 replication. *Int. J. Clin. Exp. Pathol.* **8**, 1184–1198 (2015).
53. C. Jolly, Q. J. Sattentau, Human immunodeficiency virus type 1 assembly, budding, and cell-cell spread in T cells take place in tetraspanin-enriched plasma membrane domains. *J. Virol.* **81**, 7873–7884 (2007).
54. R. D. Salter, D. N. Howell, P. Cresswell, Genes regulating HLA class I antigen expression in T-B lymphoblast hybrids. *Immunogenetics* **21**, 235–246 (1985).
55. Z. Liao, D. C. Muth, E. Eitan, M. Travers, L. N. Learman, E. Lehrmann, K. W. Witwer, Serum extracellular vesicle depletion processes affect release and infectivity of HIV-1 in culture. *Sci. Rep.* **7**, 2558 (2017).
56. D. P. Sharma, M. C. Zink, M. Anderson, R. Adams, J. E. Clements, S. V. Joag, O. Narayan, Derivation of neurotropic simian immunodeficiency virus from exclusively lymphocytetropic parental virus: Pathogenesis of infection in macaques. *J. Virol.* **66**, 3550–3556 (1992).
57. T. Arab, E. R. Mallick, Y. Huang, L. Dong, Z. Liao, Z. Zhao, O. Gololobova, B. Smith, N. J. Haughey, K. J. Pienta, B. S. Slusher, P. M. Tarwater, J. P. Tosar, A. M. Zivkovic, W. N. Vreeland, M. E. Paulaitis, K. W. Witwer, Characterization of extracellular vesicles and synthetic nanoparticles with four orthogonal single-particle analysis platforms. *J. Extracell. Vesicles* **10**, e12079 (2021).
58. M. Batish, S. Tyagi, Fluorescence in situ imaging of dendritic RNAs at single-molecule resolution. *Curr. Protoc. Neurosci.* **89**, e79 (2019).
59. A. Koppula, A. Abdelgawad, J. Guarnerio, M. Batish, V. Parashar, CircFISH: A novel method for the simultaneous imaging of linear and circular RNAs. *Cancer* **14**, 428 (2022).
60. D. Szklarczyk, A. L. Gable, D. Lyon, A. Junge, S. Wyder, J. Huerta-Cepas, M. Simonovic, N. T. Doncheva, J. H. Morris, P. Bork, L. J. Jensen, C. von Mering, STRING v11: Protein-protein association networks with increased coverage, supporting functional discovery in genome-wide experimental datasets. *Nucleic Acids Res.* **47**, D607–D613 (2019).
61. P. Langfelder, S. Horvath, WGCNA: An R package for weighted correlation network analysis. *BMC Bioinformatics* **9**, 559 (2008).
62. EV-TRACK Consortium, J. Van Deun, P. Mestdagh, P. Agostinis, Ö. Akay, S. Anand, J. Anckaert, Z. A. Martinez, T. Baetens, E. Beghein, L. Bertier, G. Berx, J. Boere, S. Boukouris, M. Bremer, D. Buschmann, J. B. Byrd, C. Casert, L. Cheng, A. Cmoch, D. Daveloose, E. De Smedt, S. Demirsoy, V. Depoorter, B. Dhondt, T. A. P. Driedonks, A. Dudek, A. Elsharawy, I. Floris, A. D. Foers, K. Gärtner, A. D. Garg, E. Geeurickx, J. Gettemans, F. Ghazavi, B. Giebel, T. G. Kormelink, G. Hancock, H. Helsmoortel, A. F. Hill, V. Hyenne, H. Kalra, D. Kim, J. Kowal, S. Kraemer, P. Leidinger, C. Leonelli, Y. Liang, L. Lippens, S. Liu, A. L. Cicero, S. Martin, S. Mathivanan, P. Mathiyalagan, T. Matusek, G. Milani, M. Monguió-Tortajada, L. M. Mus, D. C. Muth, A. Németh, E. N. M. Nolte-'t Hoen, L. O'Driscoll, R. Palmulli, M. W. Pfaffl, B. Primdal-Bengtson, E. Romano, Q. Rousseau, S. Sahoo, N. Sampaio, M. Samuel, B. Scicluna, B. Soen, A. Steels, J. V. Swinnen, M. Takatalo, S. Thaminy, C. Théry, J. Tulkens, I. Van Audenhove, S. van der Grein, A. Van Goethem, M. J. van Herwijnen, G. Van Niel, N. Van Roy, A. R. Van Vliet, N. Vandamme, S. Vanhauwaert, G. Vergauwen, F. Verweij, A. Wallaert, M. Wauben, K. W. Witwer, M. I. Zonneveld, O. De Wever, J. Vandesompele, A. Hendrix, EV-TRACK: Transparent reporting and centralizing knowledge in extracellular vesicle research. *Nat. Methods* **14**, 228–232 (2017).

Acknowledgments: We thank members of the Witwer laboratory for discussions and support. We are particularly grateful to members of the Retrovirus laboratory for access to virus strains and helpful suggestions. We acknowledge the Office of the Director and the National Institute of General Medical Sciences of the National Institutes of Health for grant S10OD023548, which supported the acquisition of electron microscopy and laser scanning confocal microscope images at the Johns Hopkins University School of Medicine Microscope Facility. Mass spectrometry was performed in the Johns Hopkins University School of Medicine Mass Spectrometry and Proteomics Core. **Funding:** This work was supported by National Institute on Drug Abuse grant DA040385 (to K.W.W.), National Institute on Drug Abuse grant DA047807 (to K.W.W.), National Science Fund for Young Scientists of China 82302637 (to Y.H.), Johns Hopkins National Institute of Mental Health Center grant MH075673 (to Y.H.), Johns Hopkins University Center for AIDS Research grant AI094189 (to Y.H.), National Science Foundation grant 2244127 (to M.B.), National Science Fund for Distinguished Young Scholars of China grant 82025024 (to L.Z.), National Key Research and Development Program of China grant 2021YFA1300604 (to L.Z.), NCI/Common Fund grant CA241694 (to K.W.W.), National Institute of Allergy and Infectious Diseases grant AI144997 (to K.W.W.), and National Institute of Mental Health grant MH118164 (to K.W.W.). **Author contributions:** Conceptualization: Y.H., K.W.W., L.Z., Z.L., and O.G. Methodology: Y.H., A.A., O.G., Z.L., M.B., L.Z., and K.W.W. Investigation: Y.H., A.A., Z.L., M.B., and O.G. Resources: K.W.W., L.Z., Y.H., Z.L., and M.B. Validation: Y.H., A.A., Z.L., K.W.W., M.B., and L.Z. Formal analysis: Y.H., X.C., A.A., and K.W.W. Software: Y.H. and X.C. Visualization: Y.H., X.C., A.A., L.Z., and O.G. Data curation: Y.H., K.W.W., L.Z., and M.B. Funding acquisition: K.W.W., L.Z., Y.H., and M.B. Supervision: K.W.W. and L.Z. Project administration: K.W.W., L.Z., and Z.L. Writing—original draft: Y.H., K.W.W., and L.Z. Writing—review and editing: K.W.W., Y.H., and M.B. **Competing interests:** K.W.W. has a sponsored research agreement with Ionis Pharmaceuticals; is or has been an advisory board member of ShiftBio, Exopharm, NeuroDex, NovaDip, and ReNeuron; holds stock options with NeuroDex; and performs ad hoc consulting as Kenneth Witwer Consulting. **Data and materials availability:** All data needed to evaluate the conclusions in the paper are present in the paper and/or the Supplementary Materials.

Submitted 24 May 2024
Accepted 6 February 2025
Published 12 March 2025
10.1126/sciadv.adq6557